



**Theoretical analysis of mixing in liquid clouds. Part IV: DSD evolution  
and mixing diagrams**

Mark Pinsky, and Alexander Khain

Department of Atmospheric Sciences, The Hebrew University of Jerusalem, Israel

Communicating author: Alexander Khain, The Hebrew University of Jerusalem,  
[khain@vms.huji.ac.il](mailto:khain@vms.huji.ac.il)



1        **Abstract**

2        Evolution of droplet size distribution (DSD) due to mixing between cloudy and dry  
3 volumes is investigated for different values of the cloud fraction and different initial DSD  
4 shapes. The analysis is performed using a diffusion-evaporation model which describes time-  
5 dependent processes of turbulent diffusion and droplet evaporation within a mixing volume.  
6 Time evolution of the DSD characteristics such as droplet concentration, liquid water content,  
7 mean volume and the effective radii is analyzed. The mixing diagrams are plotted for the final  
8 mixing stages. It is shown that the difference between the mixing diagrams for homogeneous  
9 and inhomogeneous mixing is insignificant and decreases with an increase in the DSD width.  
10 The dependencies of normalized cube of the effective radius on the cloud fraction were  
11 compared with those on normalized droplet concentration and found to be quite different. In  
12 case the normalized droplet concentration is used, mixing diagrams do not show any  
13 significant dependency on relative humidity in the dry volume.

14        The main conclusion of the study is that traditional mixing diagrams cannot serve as a  
15 reliable tool in analysis of mixing type.

16        **Keywords:** turbulent mixing, droplet evaporation, DSD evolution, mixing diagram

17



## 18      **1. Introduction**

19      This study is Part 4 of series of papers dedicated to investigation of turbulent mixing  
20 between cloud and environmental volumes. Korolev et al. (2016) (hereafter, Pt1) presented  
21 analysis of conventional (classical) concept of mixing and introduced the main parameters  
22 characterizing homogeneous and extremely inhomogeneous mixing. According to the  
23 classical concept, the final equilibrium state with RH=100% is reached either by a partial  
24 evaporation of all droplets (homogeneous mixing) or a total evaporation of a certain portion of  
25 droplets that does not affect the remaining droplets (extremely inhomogeneous mixing)  
26 (Lehmann et al., 2009; Pt1). According to this concept, at a monodisperse initial droplet size  
27 distribution (DSD), homogeneous mixing leads to a decrease in droplet size and droplet mass  
28 content, while droplet concentration remains unchanged. Extremely inhomogeneous mixing is  
29 characterized by decreasing droplet concentration due to full evaporation of droplets  
30 penetrating the initially dry air volume while the DSD shape in the cloud volume remains  
31 unchanged. As a result of extremely inhomogeneous mixing, droplet concentration decreases  
32 while the mean volume radii remain unchanged. At a polydisperse DSDs, the extreme  
33 homogeneous mixing is characterized by proportional changes in DSD for all droplet radii  
34 (Pt1). Since widely used mixing diagrams describe the final equilibrium stage of mixing they  
35 do not contain information about changes in microphysical quantities in the course of mixing.

36      Pinsky et al. (2016a, hereafter Pt2) analyzed the time evolution of monodisperse and  
37 polydisperse DSD during homogeneous mixing. It was shown that result of mixing strongly  
38 depends on the shape of the initial DSD. At a wide DSD, evaporation of droplets (first of all,  
39 the smallest ones) is not accompanied by a decrease in the effective radius. Moreover, this  
40 radius may even increase over time. This result indicates that the widely used criterion of  
41 separation of mixing types based on the behavior of the effective radius during mixing is not  
42 generally relevant and may be wrong in application to real clouds.



43 Pinsky et.al. (2016b, hereafter Pt3) introduced a diffusion-evaporation model which  
44 describes evolution DSDs and all the microphysical variables due to two simultaneously  
45 occurring processes: turbulent diffusion and droplet evaporation. Mixing between two equal  
46 volumes of subsaturated and cloudy air was analyzed, i.e. it was assumed that the cloud  
47 volume fraction  $\mu = 1/2$ . The initial DSD in the cloudy volume was assumed monodisperse.  
48 These simplified assumptions allowed to reduce the turbulent mixing equations to two-  
49 parametric ones. The first parameter is the Damköhler number,  $Da$ , which is the ratio of the  
50 characteristic mixing time to the characteristic phase relaxation time. The second parameter is  
51 the potential evaporation parameter  $R$  characterizing the ratio between the amount of water  
52 vapor needed to saturate the initially dry volume and the amount of available liquid water in  
53 the cloudy volume.

54 Within the  $Da - R$  space, in addition to the two extreme mixing types defined in the  
55 classical concept, two more mixing regimes were distinguished, namely, intermediate and  
56 inhomogeneous mixing. It was shown that any type of mixing leads to formation of a tail of  
57 small droplets, i.e. to DSD broadening. It was also shown that the relative humidity in the  
58 initially dry volume rapidly increases due to both water vapor diffusion and evaporation of  
59 penetrating droplets. As a result, the effective radii in the initially dry volume rapidly  
60 approach the values typical of cloudy volume. At the same time, the liquid water content  
61 remains significantly lower than that in the cloudy volume during much longer time than  
62 required for the effective droplet radius to grow.

63 In the present study (Pt4) we continue investigating the turbulent mixing between an  
64 initially dry volume and a cloudy volume. The focus of the study is investigation of DSD  
65 temporal evolution and analysis of the final equilibrium DSD. In comparison to Pt3, the  
66 problem analyzed in this study is more sophisticated in several aspects:



67       • The dependences of different mixing characteristics on cloud volume fraction  $0 \leq \mu \leq 1$   
68 are analyzed. In this case the equations of turbulent mixing cannot be reduced to the two-  
69 parametric problem as it was done in Pt3.

70       • The initial DSDs in cloud volume are polydisperse. We use both narrow and wide  
71 initial DSD described by Gamma distributions with different sets of parameters. The DSD are  
72 the same as those used in Pt2.

73       • The equation for supersaturation, used in this study, is valid at low humidity in the  
74 initially dry volume and is more general and compared with that used in Pt3, which makes the  
75 DSD calculations more accurate.

76       At the same time, some simplifications used in Pt3 are retained in this study. The vertical  
77 movement of the entire mixing volume is neglected; collisions between droplets and droplet  
78 sedimentation are not allowed. Also, we consider a 1D diffusion-evaporation problem. We  
79 neglect the changes of temperature in the course of mixing, which is possibly a less significant  
80 simplification. All these simplifications allow to reveal the effects of turbulent mixing and  
81 evaporation on DSD evolution.

82

## 83 **2. Formulation of the problem and model design**

84       In this study, the process of mixing is investigated basing on the solution of 1D diffusion-  
85 evaporation equation (see also Pt3). According to this equation, evaporation of droplets due to  
86 negative supersaturation in the mixing volume takes place simultaneously with turbulent  
87 mixing. Since droplets within the volume are under different negative supersaturation values  
88 until the final equilibrium is reached, the modeled mixing is inhomogeneous. The droplets can  
89 evaporate either partially or totally. The evaporation leads to a decrease in droplet sizes and in  
90 droplet concentration.

91       Like in Pt3, the process of turbulent diffusion is described by a 1D equation of turbulent  
92 diffusion with a turbulent coefficient  $K$ . The mixing is assumed to be driven by isotropic



93 turbulence at scales within the inertial sub-range where Richardson's law is valid. In this case,  
94 turbulent coefficient is evaluated as in Monin and Yaglom (1975).

$$95 \quad K(L) = C\varepsilon^{1/3}L^{4/3} \quad (1)$$

96 In Eq. (1)  $\varepsilon$  is the turbulent kinetic energy dissipation rate and  $C = 0.2$  is a constant (Monin  
97 and Yaglom, 1975), Boffetta and Sokolov (2002). Eq. (1) means that we consider the effects  
98 of turbulent diffusion at scales much larger than the Kolmogorov microscale, i.e. the effects of  
99 molecular diffusion are neglected. In the simulations, we use  $L = 40 \text{ m}$  and  $\varepsilon = 20 \text{ cm}^2 \text{ s}^{-3}$ .

100

### 101 *Geometry of mixing and the initial conditions*

102 The conceptual scheme presenting mixing geometry and the initial conditions used in the  
103 following analysis are shown in **Figure 1**.

104

### 105 **Fig 1 here**

106

107 At  $t = 0$  the mixing volume of length  $L$  is divided into two volumes: the cloud volume of  
108 length  $\mu L$  (Fig.1, left) and the dry volume of length  $(1 - \mu)L$  (Fig.1, right), where  $0 \leq \mu \leq 1$   
109 is the cloud volume fraction. The entire volume is assumed closed, i.e. adiabatic. At  $t = 0$  the  
110 cloud volume is assumed saturated, so the supersaturation  $S_1 = 0$ . This volume is also  
111 characterized by the initial distribution of the square of the droplet radii  $g_1(\sigma)$ , where  $\sigma = r^2$ .

112 The initial liquid water mixing ratio in the cloudy volume is equal to

$$113 \quad q_{w1} = \frac{4\pi\rho_w}{3\rho_a} \int_0^\infty \sigma^{3/2} g_1(\sigma) d\sigma. \text{ The integral of } g_1(\sigma) \text{ over } \sigma \text{ is equal to the initial droplet}$$

$$114 \quad \text{concentration in the cloud volume } N_1 = \int_0^\infty g_1(\sigma) d\sigma. \text{ The initial droplet concentration in the}$$

115 dry volume is  $N_2 = 0$ , the initial negative supersaturation in this volume is  $S_2 < 0$  and the



116 initial liquid water mixing ratio  $q_{w2} = 0$ . Therefore, the initial profiles of these quantities  
 117 along the  $x$ -axis are step functions:

118

$$119 \quad N(x, 0) = \begin{cases} N_1 & \text{if } 0 \leq x < \mu L \\ 0 & \text{if } \mu L \leq x < L \end{cases} \quad (2a)$$

$$120 \quad S(x, 0) = \begin{cases} 0 & \text{if } 0 \leq x < \mu L \\ S_2 & \text{if } \mu L \leq x < L \end{cases} \quad (2b)$$

$$121 \quad q_w(x, 0) = \begin{cases} q_{w1} & \text{if } 0 \leq x < \mu L \\ 0 & \text{if } \mu L \leq x < L \end{cases} \quad (2c)$$

122

123 The initial profile of droplet concentration is shown in Fig. 1b. This is the simplest  
 124 inhomogeneous mixing scheme, wherein mixing takes place only in the  $x$ -direction, and the  
 125 vertical velocity is neglected.

126 Since the total volume is adiabatic, the fluxes of different quantities through the left and  
 127 right boundaries at any time instance are equal to zero, i.e.

128

$$129 \quad \frac{\partial N(0, t)}{\partial x} = \frac{\partial N(L, t)}{\partial x} = 0; \quad \frac{\partial q_w(0, t)}{\partial x} = \frac{\partial q_w(L, t)}{\partial x} = 0; \quad \frac{\partial q_v(0, t)}{\partial x} = \frac{\partial q_v(L, t)}{\partial x} = 0 \quad (3)$$

130 where  $q_v$  is the water vapor mixing ratio.

131 To investigate of mixing process for different initial DSD, we assume that DSD in the cloud  
 132 volume can be represented by a Gamma distribution:

$$133 \quad f(r, t = 0) = \frac{N_0}{\Gamma(\alpha)\beta} \left(\frac{r}{\beta}\right)^{\alpha-1} \exp\left(-\frac{r}{\beta}\right) \quad (4)$$

134 where  $N_0$  is an intercept parameter,  $\alpha$  is a shape parameter and  $\beta$  is a slope parameter of  
 135 distribution. The DSD  $f(r)$  relates to distribution  $g_1(\sigma)$  as  $f(r) = 2rg_1(\sigma)$ . We performed  
 136 simulations with both initially wide and narrow DSDs. The width of DSD is determined by a  
 137 set of parameters. The parameters of the initial Gamma distributions used in this study are



138 presented in **Table 1**. Parameters of the distributions are chosen in such a way that the modal  
139 radii of DSD and the values of LWC are the same for both distributions. These distributions  
140 were used in Pt2 for analysis of homogeneous mixing.

141

142 **Table 1 here**

143

144

145 *Conservative quantity*  $\Gamma(x,t)$

146 The supersaturation equation for an adiabatic immovable volume can be written in the

147 form  $\frac{1}{S+1} \frac{dS}{dt} = -A_2 \frac{dq_w}{dt}$ , where  $S$  is supersaturation over water, and the coefficient

148  $A_2 = \frac{1}{q_v} + \frac{L_w^2}{c_p R_v T^2}$  is slightly dependent on temperature (Korolev and Mazin, 2003) (notations

149 of other variables are presented in **Appendix**). In our analysis we consider  $A_2$  to be a

150 constant. As follows from the supersaturation equation, the quantity

151

$$152 \Gamma(x,t) = \ln[S(x,t)+1] + A_2 q_w(x,t) \quad (5)$$

153

154 is a conservative quantity, i.e. invariant with respect to phase transitions. In Eq. (5),  $|S(x,t)|$

155 can be comparable with unity by the order of magnitude. The conservative quantity  $\Gamma(x,t)$

156 obeys the following equation for turbulent diffusion

157

$$158 \frac{\partial \Gamma(x,t)}{\partial t} = K \frac{\partial^2 \Gamma(x,t)}{\partial x^2} \quad (6)$$

159



160 with the adiabatic (no flux) condition at the left and right boundaries  $\frac{\partial \Gamma(0,t)}{\partial x} = \frac{\partial \Gamma(L,t)}{\partial x} = 0$

161 and the initial profile at  $t = 0$

162

$$163 \quad \Gamma(x,0) = \begin{cases} A_2 q_{w1} & \text{if } 0 \leq x < \mu L \\ \ln[S_2 + 1] & \text{if } \mu L \leq x < L \end{cases} \quad (7)$$

164

165 From Eq. (7) it follows that  $\Gamma(x,0)$  is positive in the cloud volume and negative in the

166 initially dry volume. The mean value of function  $\Gamma(x,0)$  can be written as follows:

167

$$168 \quad \bar{\Gamma} = \frac{1}{L} \int_0^L \Gamma(x,0) dx = \frac{A_2 q_{w1}}{L} \int_0^{\mu L} dx + \frac{\ln[S_2 + 1]}{L} \int_{\mu L}^L dx = \mu A_2 q_{w1} + (1 - \mu) \ln[S_2 + 1] \quad (8)$$

169

170  $\bar{\Gamma}$  can be either positive or negative. In the latter case a complete evaporation of droplets in the

171 course of mixing takes place.

172 The solution of Eq. (6) with the initial condition (7) is (Polyanin et al., 2004):

$$173 \quad \Gamma(x,t) = \sum_{n=0}^{\infty} a_n \exp\left(-\frac{Kn^2 \pi^2 t}{L^2}\right) \cos\left(\frac{n\pi x}{L}\right) =$$

$$\mu A_2 q_{w1} + (1 - \mu) \ln[S_2 + 1] -$$

$$2(\ln[S_2 + 1] - A_2 q_{w1}) \sum_{n=1}^{\infty} \frac{\sin(n\pi\mu)}{n\pi} \exp\left(-\frac{Kn^2 \pi^2 t}{L^2}\right) \cos\left(\frac{n\pi x}{L}\right) \quad (9)$$

174 One can see that function  $\Gamma(x,t)$  depends on three independent parameters  $A_2 q_{w1}$ ,  $S_2$  and  $\mu$ .

175 This function does not depend on the shape of the initial DSD in the cloud volume. In the final

176 state when  $t \rightarrow \infty$ ,  $\Gamma(x,t)$  is :

$$177 \quad \Gamma(t = \infty) = \mu A_2 q_{w1} + (1 - \mu) \ln[S_2 + 1] \quad (10)$$

178 Therefore,  $\Gamma(t = \infty)$  depends on the cloud fraction and the initial values of liquid water

179 mixing ratio in the cloud volume and the relative humidity in initially dry volume.



180 The final equilibrium values of supersaturation  $S(x, \infty)$  and liquid water mixing ratio  
181  $q_w(x, \infty)$  can be calculated using Eq. (5). The case  $\Gamma(t = \infty) > 0$  corresponds to the  
182 equilibrium state with  $S(x, \infty) = 0$  and  $q_w(x, \infty) = \mu q_{w1} + (1 - \mu) \frac{\ln[S_2 + 1]}{A_2}$ . The case  
183  $\Gamma(t = \infty) < 0$  corresponds to the equilibrium state with  $q_w(x, \infty) = 0$  and  
184  $S(x, \infty) = (1 + S_2)^{1-\mu} \exp(\mu A_2 q_{w1}) - 1$ . At given  $q_{w1}$  and  $S_2$ , there is a critical value of the  
185 cloud fraction  $\mu_{cr}$  which separates these two possible final equilibrium states. This critical  
186 value corresponds to  $\Gamma(t = \infty) = 0$  and can be calculated from Eq. (10) as:

187

$$188 \quad \mu_{cr} = \frac{\ln[S_2 + 1]}{\ln[S_2 + 1] - A_2 q_{w1}} \quad (11)$$

189

190 Another expression for  $\mu_{cr}$  was formulated in Pt1.

191 The examples of spatial-temporal variations of function  $\Gamma(x, t)$  for different cloud  
192 fractions and initial RH=80% are shown in **Figure 2**.

193

194 **Fig 2 here**

195

196 Upper panels  $\mu = 0.1$  correspond to the case of final total droplet evaporation and negative  
197 final function  $\Gamma$ , whereas the middle and bottom rows  $\mu = 0.5$  and  $\mu = 0.9$  illustrate partial  
198 evaporation cases when the total mixing volume reaches saturation. It is interesting that the  
199 time required for the final equilibrium state to be reached practically does not depend on the  
200 cloud fraction, being ~180 seconds for the illustrated cases. The cases  $\mu = 0.1$  and  $\mu = 0.9$   
201 demonstrate a strong non-symmetric spatial variability of  $\Gamma(x)$  function during the first 50  
202 seconds. At  $\mu = 0.5$ , a nearly full compensation between saturation deficit in the dry



203 volume and available liquid water in the cloud volume takes place if at the equilibrium state

204  $S(x, \infty) = q_w(x, \infty) = \Gamma(x, \infty) = 0$ . However, the compensation at  $\mu = 0.5$  is not full because of

205 the nonlinearity of  $\Gamma$  in Eq. (5).

206

### 207 *Diffusion-evaporation equation for DSD*

208 To formulate the diffusion-evaporation equation we use a simplified equation for droplet

209 evaporation (Pruppacher and Klett, 1997), in which the curvature term and the chemical

210 composition term are omitted

$$211 \quad \frac{d\sigma}{dt} = \frac{2S}{F} \quad (12)$$

212 where  $F = \frac{\rho_w L_w^2}{k_a R_v T^2} + \frac{\rho_w R_v T}{e_w(T) D} = \text{const}$  (Notations of other variables are presented in Appendix.)

213 The solution of Eq. (12) is

$$214 \quad \sigma(t) = \frac{2}{F} \int_0^t S(t') dt' + \sigma_0 \quad (13)$$

215 Eq. (13) means that in the course of evaporation, distribution  $g(\sigma)$  shifts to the left without

216 changing its shape. The diffusion-evaporation equation for function  $g(x, t, \sigma)$  can be written

217 in the form

218

$$219 \quad \frac{\partial g}{\partial t} = K \frac{\partial^2 g}{\partial x^2} + \frac{\partial}{\partial \sigma} \left( \frac{d\sigma}{dt} g \right) \quad (14)$$

220 Combining Eqs. (12) and (14) yields

$$221 \quad \frac{\partial g(x, t, \sigma)}{\partial t} = K \frac{\partial^2 g(x, t, \sigma)}{\partial x^2} + \frac{2S}{F} \frac{\partial g(x, t, \sigma)}{\partial \sigma} \quad (15)$$

222

223 Eq. (15) is similar to the diffusion-evaporation equation for size distribution function used in

224 Pt 3. The first term on the right hand side of Eq. (15) describes the effect of turbulent



225 diffusion, while the second term describes the changes of size distribution due to droplet  
 226 evaporation. To close this equation, one can use Eq. (5) written as

227

$$228 \quad S(x, t) = \exp[\Gamma(x, t) - A_2 q_w(x, t)] - 1, \quad (16)$$

229

230 and the equation for liquid water mixing ratio

231

$$232 \quad q_w(x, t) = \frac{4\pi\rho_w}{3\rho_a} \int_0^\infty \sigma^{3/2} g(x, t, \sigma) d\sigma \quad (17)$$

233 The equation system (15-17) for distribution  $g(x, t, \sigma)$  should be solved under the following

234 initial condition

$$235 \quad g(x, 0, \sigma) = \begin{cases} g_1(\sigma) & \text{if } 0 \leq x < \mu L \\ 0 & \text{if } \mu L \leq x < L \end{cases} \quad (18)$$

236 and using the Neumann boundary conditions

237

$$238 \quad \frac{\partial g(0, t, \sigma)}{\partial x} = \frac{\partial g(L, t, \sigma)}{\partial x} = 0 \quad (19)$$

239

240 These equations were solved numerically on a linear grid of droplet radii  $r_j$  being within

241 the range 0-50  $\mu\text{m}$ , where  $j = 1 \dots 50$  are the bin numbers. The number of grid points along the

242  $x$ -axis was set equal to 81. In numerical calculations, the “evaporation term” in Eq. (15) was

243 approximated as

$$244 \quad \frac{2S}{F} \frac{\partial g(x, t, \sigma)}{\partial \sigma} \approx \frac{g\left(x, t, \sigma + \frac{2S}{F} \Delta t\right) - g(x, t, \sigma)}{\Delta t}. \quad (20)$$

245



246 A shift and subsequent remapping of DSD using the method proposed by Kovetz and Olund's  
247 (1969) were implemented to solve Eq. (20) with the help of MATLAB solver PDEPE. After  
248 calculation of  $g(x, t, \sigma_j)$  function, DSD  $f(x, t, r_j)$  was calculated using the relationship  
249  $f(x, t, r_j) = 2r_j g(x, t, \sigma_j)$ .

250

### 251 3. Spatial-temporal variations of DSD and of DSD parameters

252 Mixing may take a significant time. Cloud microphysical parameters measured in *in-situ*  
253 observations correspond to different stages of this transient mixing process. During mixing,  
254 DSDs and its parameters change substantially, which makes it reasonable to analyze these  
255 time changes.

256 **Figure 3** shows time evolution of initially narrow DSD in the centers of the cloudy volume  
257 and of the initially dry volume. The values of DSD in the initially cloudy volume decrease  
258 while there are no significant changes in the DSD shape. At  $\mu = 0.7$ , the droplet radius  
259 corresponding to the DSD maximum remains unchanged during mixing staying equal to 10  
260  $\mu\text{m}$ . At  $\mu = 0.3$  the effect of droplet diffusion on DSD is stronger, and mixing leads not  
261 only to a decrease in the DSD values, but also to a decrease in the peak droplet radius in the  
262 cloudy volume. Both at  $\mu = 0.3$  and  $\mu = 0.7$ , mixing leads to broadening of the initial DSD  
263 due to the appearance of the tail of small droplets.

264 In the center of the initially dry volume, the rate of the DSD growth depends on the value  
265 of the cloud fraction. At a low cloud fraction, DSD maximum remains substantially lower for  
266 the most period of mixing than that in the cloudy volume. At the same time, the radius  
267 corresponding to the DSD maximum increases reaching 80% of its maximum value already  
268 within the first 5 s. This is due to the fast increase in the relative humidity during mixing, so  
269 large droplets penetrating the initially dry volume do not decrease in size anyhow significantly  
270 determining the values of modal, mean volume and effective radii.

271



272 **Figure 3 here**

273

274 At the initially wide DSD (**Figure 4**), the radii of the DSD maximum do not change. It  
275 means that at the initial RH= 80%, mixing and evaporation leads to a fast saturation of the  
276 initially dry volume, after which the peak radius remains unchanged.

277

278

279 **Figure 4 here**

280

281

282 It is interesting that at  $\mu=0.3$  in the initially dry volume, DSD reaches its maximum during  
283 the transition period (Fig.4, at  $t=80s$ ), and then decreases toward the equilibrium state. This  
284 behavior is caused by the competition between the diffusion and droplet evaporation.

285 **Figure 5** shows spatial dependences of droplet concentration, LWC and the effective  
286 radius within the mixing volume at different time instances at narrow initial DSD. At small  
287 values of the cloud fraction, diffusion of water vapor and droplets, as well as droplet  
288 evaporation lead to a fast decrease in droplet concentration and in LWC in the initially cloud  
289 volume. The effective radius in this volume decreases by about 12% in the course of mixing.

290 It is natural that at large cloud fraction, droplet concentration and LWC in the initially cloudy  
291 volume decrease slowly, while these quantities in the initially dry volume increase rapidly At  
292 both small and large cloud fractions, the effective radius in the initially dry volume grows  
293 rapidly during the mixing toward its values in the initially cloudy volumes, even if droplet  
294 concentration and LWC remain much lower than in the cloud volume.

295

296 **Figure 5 here**

297



298 **Figure 6** shows the spatial dependences of droplet concentration, LWC and the effective  
299 radius within the mixing volume at different time instances at wide initial DSD.

300

301

302 **Figure 6 here**

303

304

305 A specific feature of mixing at a wide DSD is the increase in the effective radius, so the ratio

306  $\frac{r_e}{r_{e0}} > 1$ . In the course of mixing, the effective radius maximum is reached in the initially dry

307 volumes. This result can be attributed to the fact that in this volume smaller droplets fully

308 evaporate, so the concentration of large droplets increases with respect to concentration of

309 smaller droplets (Fig. 4, right column). Scattering diagrams plotted using *in-situ* observations

310 often contain points or groups of points with  $\frac{r_e}{r_{e0}} > 1$  (e.g. , Burnet and Brenguier, 2007;

311 Krueger et al., 2006, Gerber et al., 2008). In these observations, the effective radius was

312 measured within the cloud volume with maximum liquid water content (i.e. less diluted). The

313 result obtained in the present study shows that the behavior of  $\frac{r_e}{r_{e0}}$  with time in the course of

314 mixing may depend of the DSD shape in the initially cloud volume.

315 We see that the transition to the final equilibrium state within the volume with the spatial

316 scale of 40 m is about 5 min (Fig. 8), which is a comparatively long period of time compared

317 to the characteristic times of other microphysical processes, including droplet evaporation.

318 During this time the DSD changes substantially, especially at a small cloud fraction. The

319 effective radius in the initially dry volume increases much faster than LWC, reaching the

320 values typical of cloudy air at the time instance when LWC is still substantially lower than in

321 the cloudy volume. Despite some DSD broadening, the final DSD in the mixing volume



322 resemble those in the initially cloud volume. The main effect of mixing is lowering the DSD  
323 values as the cloud fraction decreases.

324

325

#### 326 **4. Equilibrium state and mixing diagram**

327 Mixing considered in the present study always leads to the equilibrium state. As was  
328 explained above, two equilibrium states are possible. The first one is characterized by the total  
329 evaporation of cloud droplets  $q_w(x, \infty) = 0$ , whereas the second one occurs at saturation of  
330 the total volume, i.e.  $S(x, \infty) = 0$ . At the given initial values of  $q_{w1}$  in the cloud volume and of  
331  $S_2$  in the initially dry volume, there always exists the cloud fraction  $\mu_{cr}$  (Eq. 11) separating  
332 these two regimes.

##### 333 **4.1. The process of achieving the equilibrium state**

334 **Figure 7** shows the dependences of the time required to reach the equilibrium on the cloud  
335 fraction, at different initial relative humidity values in the dry volume and two initial DSDs  
336 (the parameters are presented in Tab.1). The characteristic time is defined here as the time  
337 from the beginning of mixing to the time instance when inequality  $\delta = \frac{\bar{N}(t) - \bar{N}(\infty)}{\bar{N}(0) - \bar{N}(\infty)} < 0.01$

338 becomes valid. The mean droplet concentration is calculated by averaging along  $x$ -axes

339  $(\bar{N}(t) = \frac{1}{L} \int_0^L N(x, t) dx)$ . In case of a total evaporation,  $\bar{N}(\infty) = 0$ .

340

341 **Figure 7 here**

342

343 Each curve in Fig. 7 consists of two branches. The left branches correspond to the total  
344 evaporation regime, while the right branches correspond to the partial evaporation at  
345 equilibrium. The maximum time corresponds to the situation when the available amount of



346 liquid water is approximately equal to the saturation deficit. A similar result was obtained in  
347 Pt1 and Pt2 for homogeneous mixing. The maximum values of the characteristic time are  
348 about 4 min for a mixing volume of 40 m in length. The right branches show that the  
349 characteristic time decreases with increasing cloud fraction. Despite some differences in the  
350 curve slopes, the characteristic times for wide and narrow DSD are quite similar.

351 **Figure 8** shows dependences of normalized cube of the effective radius on the cloud  
352 fraction at different time instances for two values of  $x$ :  $x = 0$  (solid lines) corresponds to the  
353 initially cloudy volume, and  $x = L$  (dashed line) corresponds to the initially dry volume. The  
354 figure is plotted for the narrow DSD for two values of  $RH_2$ : 60% and 95%.

355

356 **Figure 8 here**

357

358 The curve plotted for the time instance of 300 s corresponds to the equilibrium state (hereafter the  
359 equilibrium curve). The curves above the equilibrium curve correspond to the initially cloudy  
360 volume, and the curves below the equilibrium curve correspond to the initially dry volume. One  
361 can see how curves of both types approach the same final state. During the mixing the curves

362 move over the  $\left(\frac{r_e}{r_{e0}}\right)^3 - \mu$  plane toward the equilibrium curve. As a result, the curves plotted in

363 Fig.8, corresponding to different time instances of the mixing, together cover the entire area of the  
364 panels.

365 . During this movement the distance from the curves to the horizontal line  $\left(\frac{r_e}{r_{e0}}\right)^3 = 1$

366 changes, and the curves slopes increase. In our case of  $L = 40$  m, the mixing remains  
367 inhomogeneous during entire mixing process, so the change in the distance from the



368 curves to the horizontal line  $\left(\frac{r_e}{r_{e0}}\right)^3 = 1$  characterizes the temporal changes over the mixing  
369 process, but not a change in mixing type.

370 It is noteworthy in this relation that scattering diagrams plotted using *in-situ* observations  
371 reflect mixing between different multiple volumes at different stages of the mixing process.  
372 Accordingly, points in the scattering diagrams can be far from the equilibrium location. Fig. 8  
373 indicates, therefore, that scattering diagrams show snapshots of transient mixing process when

374 the distance from points in the diagrams to line  $\left(\frac{r_e}{r_{e0}}\right)^3 = 1$  characterize the stage of the  
375 mixing process, but not the mixing type.

376 The dependences of normalized cube of the effective radius on the cloud fraction at different  
377 time instances at wide DSD also indicate approaching to the equilibrium curve, while all the

378 curves correspond to  $\left(\frac{r_e}{r_{e0}}\right)^3 > 1$  (not shown).

#### 379 4.2. Mixing diagrams

380 Using the diffusion-evaporation equations (15-17) we calculated the equilibrium DSD for  
381 different initial relative humidity values and different cloud fractions. Each calculation was  
382 performed for both narrow and wide initial DSD (parameters shown in Tab.1). These  
383 equilibrium DSD were used to calculate mixing diagrams showing dependences of normalized  
384 cube of the effective radius on the cloud fraction.

385 The corresponding mixing diagrams for homogeneous mixing case were also calculated  
386 for comparison. To this effect, the supersaturation and DSD in both the cloud and the dry  
387 volumes were aligned, taking into account the cloud fraction value  $\mu$ . The alignment led to  
388 the following initial values of supersaturation and DSD within the mixing volume:

389

$$390 S_0 = (1 - \mu)S_2; \quad g_0(\sigma) = \mu g_1(\sigma) \quad (21)$$



391

392 Upon the alignment, time evolution values of DSD under homogeneous evaporation in an  
393 adiabatic immovable parcel were calculated until the equilibrium state was reached. These  
394 equilibrium DSD were used to calculate mixing diagrams for homogeneous mixing. To do  
395 this, we used the parcel model proposed by Korolev (1995) that describes evaporation by  
396 means of equations with temperature-dependent parameters. **Figure 9** shows the mixing  
397 diagrams plotted for initial narrow and wide DSD cases.

398

399 **Figure 9 here**

400 While all the curves in the mixing diagram for narrow DSD are below the straight line

401  $\left(\frac{r_e}{r_{e0}}\right)^3 = 1$ , the curves for wide DSD are above this line. The explanation of this effect is given

402 in Section 3 (Fig. 6). The curves plotted for homogeneous and inhomogeneous mixing

403 demonstrate an important feature. Namely, at given values of RH and  $q_{w1}$  in the initially dry404 volume, the values  $\mu_{cr}$  of the cloud fraction at which all the droplets evaporate are

405 approximately the same for any type of mixing. This condition is the consequence of the mass

406 conservation law determined by Eq. (11) and does not depend of the initial DSD shape. In

407 standard mixing diagrams (e.g. Lehmann et al., 2009; Gerber et al., 2008; Freud et al., 2011),

408 the horizontal straight line  $\left(\frac{r_e}{r_{e0}}\right)^3 = 1$  is typically plotted for the entire range of the cloud

409 fraction [0...1], while the curves corresponding to homogeneous mixing are plotted for

410 different RH within the range  $[\mu_{cr}(RH_2)...1]$ . As a result, the high difference between

411 extremely inhomogeneous and homogeneous mixing types is clearly seen at low RH and at

412 small cloud fractions. The condition that  $\mu_{cr}$  is the same for different mixing types indicates413 that the mixing diagrams may look nearly similar for  $\mu > \mu_{cr}$ . It means that the range of the



414 cloud fractions required for comparison of diagrams aimed at determination of a mixing type  
415 shortens as  $RH_2$  values in the surrounding air decrease.

416 The comparison of the left and the right panels in Fig. 9 shows that the differences  
417 between the diagrams for homogeneous and inhomogeneous mixing types are more  
418 pronounced for initially narrow DSD. The maximum difference should take place for  
419 monodisperse DSD considered in in Pt1, Pt2 and Pt3. Within the range of  $\mu > \mu_{cr}$ , the  
420 distance between the curves corresponding to different mixing regimes is small even for  
421 narrow DSD and low  $RH_2$ . The lower difference is related to the fact that at high  $RH_2$  the  
422 curves in the mixing diagrams are close to the horizontal straight line in both regimes, while at  
423 low  $RH_2$ ,  $\mu_{cr}$  is small and both curves should drop to zero in the vicinity of  $\mu = \mu_{cr}$ .

424 As regards the wide DSD case, the difference between the curves corresponding to  
425 different mixing type is negligible (Fig. 9, right)

426

#### 427 **4.3. Effect of the relative humidity on mixing diagram pattern**

428 In measurements carried out at cloud boundaries and in cloud simulations, the cloud  
429 fraction is not known, therefore it is widely accepted to use normalized droplet concentration  
430 instead of the cloud fraction (Burnet and Brenguier, 2007; Gerber et al., 2008; Lehmann et al.,  
431 2009). Droplet concentration is normalized by the maximum value along the airplane traverse.  
432 The difference between the cloud fraction and normalized droplet concentration is obvious:  
433 the cloud fraction is a parameter given as the initial condition. At the same time, normalized  
434 droplet concentration changes with time and space due to complete evaporation of some  
435 droplet fraction. **Figure 10** shows dependencies of normalized droplet concentration on the  
436 cloud fraction at the equilibrium final state of mixing. One can see a substantial deviation  
437 from 1:1 linear dependence, especially at low RH. As we know, droplet concentration  
438 decreases in the course of both homogeneous and inhomogeneous mixing if the initial DSD  
439 are polydisperse. The fraction of totally evaporating droplets increases with decreasing  $RH_2$ .



440 As expected, droplet concentration in homogeneous mixing is higher than that in  
441 inhomogeneous mixing. The difference between droplet concentrations at wide DSD is lower  
442 than at narrow DSD.

443

444 **Fig. 10 here**

445

446 **Figure 11** shows the dependencies  $\left(\frac{r_e}{r_{e0}}\right)^3$  on normalized droplet concentration for narrow

447 and wide DSD in inhomogeneous mixing. The normalization by droplet concentration in the  
448 initially cloud volume at  $t=0$  was used. Taking into account the dependences of normalized  
449 droplet concentration on the cloud fraction  $\mu$  (Fig. 10), one can get the curves shown in Fig.  
450 11 which actually coincide at different  $RH_2$ . The lack of the sensitivity to  $RH_2$  can be  
451 attributed to the fact that a decrease in RH leads to a decrease in normalized droplet  
452 concentration, so the curves corresponding to low RH in Fig. 9 shift to the left when the  
453 normalized droplet concentration is used instead of  $\mu$ . The shape of the dependences in Fig  
454 11 (right) is explained by an increase in the effective radius with decreasing droplet  
455 concentration.

456

457 **Fig 11 here**

458 Thus, the mixing diagrams plotted in the plane  $\left(\frac{r_e}{r_{e0}}\right)^3$  vs normalized droplet

459 concentration do not depend on the relative humidity of the surrounding dry air. This result  
460 indicates an additional difficulty in distinguishing between mixing types based on scattering  
461 diagrams plotted using *in-situ* data in these axes. The concentration of observed points in

462 these scattering diagrams close to the line  $\left(\frac{r_e}{r_{e0}}\right)^3 = 1$  is often interpreted as an indication of



463 homogeneous mixing, but at high RH in the surrounding air (Gerber et al., 2008; Lehmann et  
464 al., 2009). High values of RH in the penetrating air volumes are usually explained by  
465 formation of a layer of moist air around the cloud boundary (Gerber et al., 2008, Knight and  
466 Miller, 1998).

467 The reference values of droplet concentration and the effective radius used for  
468 normalization in the present study are taken as the initial values in the cloud volume before it  
469 mixes with the neighbouring dry volume. In real *in-situ* measurements the reference values of  
470 these quantities are typically chosen in a less diluted cloud volume along the airplane traverse.

471 This reference volume may be quite remote from the particular mixing volume. It can lead to

472 a shift of the mixing diagram with respect to the  $\left(\frac{r_c}{r_{e0}}\right)^3 = 1$  line, as well as to a large variation

473 in mixing diagram shapes, unrelated, however, to the mixing type (e.g., Lehmann et al.,  
474 2009).

475

## 476 5. Discussion and conclusion

477 This study extends the analysis of mixing performed in Pt3 where the diffusion-  
478 evaporation equation served as the basis, the initial DSD were assumed monodisperse and  
479 the cloud fraction was chosen as  $\mu = 1/2$ . In the present study, the analysis focuses on the  
480 temporal and spatial evolution of initially polydisperse DSD and investigates mixing diagrams  
481 obtained for narrow and wide initial DSD within a wide range of the cloud fraction values (  
482 0.1 - 0.95). It is shown that results of mixing and the structure of mixing diagrams depend on  
483 the initial DSD shape. This finding indicates that mixing is a multi-parametrical problem that  
484 cannot be determined by a single parameter (e.g. the Damköhler number as often assumed) or  
485 even by two parameters (the Damköhler number and the potential evaporation parameters as  
486 assumed in Pt3). The temporal changes of DSD and their moments during mixing are  
487 calculated. Although DSD broaden, they tend to remain similar to the original DSD. The main



488 changes come from the cloud air dilution by the dry air, which leads to a decrease in droplet  
489 concentration for all droplet sizes. The changes of DSD and its shape are minimum in the  
490 initially cloud volumes, especially at significant cloud fractions. The droplet radii  
491 corresponding to the DSD peak do not change anyhow significantly. In the initially dry  
492 volumes, mixing leads to a rapid increase in RH. Consequently, large droplets penetrating  
493 these volumes do not change their sizes significantly. As a result, the effective radius in these  
494 volumes rapidly increases and reaches the values typical of cloud volumes, while LWC  
495 remains lower than in the cloud volume for most of the mixing time. At narrow DSD, the  
496 effective radius remains smaller than that in the initially cloud volume. At wide DSD, the  
497 effective radius may become larger than that in the initial DSD. This increase in the effective  
498 radius is attributed to the fact that evaporation of smaller droplets leads to the increase in the  
499 fraction of larger droplets in the DSD.

500 Dependences of normalized cube of the effective radius on the cloud fraction  $(r_e / r_{e0})^3$  as  
501 a function of  $\mu$  at different time instances form the set of curves filling the entire  
502  $(r_e / r_{e0})^3 - \mu$  plane. Therefore, both the slope and the distance of these curves in respect to  
503 the horizontal line  $(r_e / r_{e0})^3 = 1$  change with time. It means that this distance characterizes  
504 the temporal changes in the course of mixing, but not the mixing type (which remains  
505 inhomogeneous during the entire mixing time). The mixing process is comparatively long  
506 (several minutes), so the final equilibrium stage is hardly achievable in real clouds.

507 It is highly significant that the critical values of the cloud fraction  $\mu_{cr}$  corresponding to  
508 total droplet evaporation are the same for any mixing type. It means that the curves in a  
509 mixing diagram corresponding to homogeneous and inhomogeneous mixing types should be  
510 compared only within the range of  $\mu > \mu_{cr}$ . The range width of  $\mu > \mu_{cr}$  decreases with  
511 decreasing relative humidity in the initially dry volume. Taking into account significant



512 scattering of observed points, this condition greatly hampers the problem of how to  
513 distinguish between mixing types,

514 Another important result of the study is that mixing diagrams for homogeneous and  
515 inhomogeneous mixing plotted for *polydisperse* DSD do not differ much. The largest  
516 difference takes place for initially narrow DSD (the maximum difference should take place for  
517 initial monodisperse DSD), but even in this case the difference is not large enough to reliably  
518 distinguish mixing type due to the significant scatter of observed data. At wide DSD, this  
519 difference becomes negligibly small.

520 The cloud fraction  $\mu$  is a predefined parameter and is not determined from observations.  
521 Consequently, in the analysis of *in-situ* measurements the normalized droplet concentration is  
522 typically used instead of the cloud fraction. However, there is a significant difference between  
523 the cloud fraction prescribed a priori and the normalized droplet concentration that changes  
524 due to total evaporation of some fraction of droplets. We have shown that utilization of  
525 normalized droplet concentration in mixing diagrams is not equivalent to utilization of the  
526 cloud fraction. The important conclusion is that when mixing diagrams are plotted using the  
527 normalized concentration, the dependence on the RH disappears. This conclusion is valid even  
528 when the RH in the initially dry volume is as low as 60%. This conclusion clearly contradicts  
529 the wide-spread assumption that mixing types can be easily distinguished in mixing diagrams  
530 in case of low relative humidity of the surrounding air.

531 To sum up, our general conclusion is that the simplifications underlying the classical  
532 concept of mixing are too crude, making it impossible to use mixing diagrams for  
533 comprehensive analysis of mixing and especially for determination of the mixing type. At the  
534 same time, mixing diagrams may contain useful information on DSD width.

535

536 *Acknowledgements*



537 This research was supported by the Israel Science Foundation (grant 1393/14), the Office  
 538 of Science (BER), the US Department of Energy Award DE-SC0006788 and the Binational  
 539 US-Israel Science Foundation (grant 2010446).

540

541

542 **Appendix. List of symbols**

Symbol	Description	Units
$A_2$	$\frac{1}{q_v} + \frac{L_w^2}{c_p R_v T^2}$ , coefficient	-
$a_n$	Fourier series coefficients	-
$C$	Richardson's law constant	-
$c_p$	specific heat capacity of moist air at constant pressure	$\text{J kg}^{-1}\text{K}^{-1}$
$D$	coefficient of water vapor diffusion in air	$\text{m}^2 \text{s}^{-1}$
$Da$	<i>Damköhler</i> number	-
$e$	water vapor pressure	$\text{N m}^{-2}$
$e_w$	saturation vapor pressure above flat surface of water	$\text{N m}^{-2}$
$F$	$\left( \frac{\rho_w L_w^2}{k_a R_v T^2} + \frac{\rho_w R_v T}{e_w(T) D} \right)$ , coefficient	$\text{m}^{-2} \text{s}$
$f(r)$	droplet size distribution	$\text{m}^{-4}$
$g(r)$	droplet size distribution	$\text{m}^{-5}$
$g_0(\sigma)$	initial distribution of square radius in homogeneous mixing	$\text{m}^{-5}$
$g_1(\sigma)$	initial distribution of square radius	$\text{m}^{-5}$
$k_a$	coefficient of air heat conductivity	$\text{J m}^{-1}\text{s}^{-1}\text{K}^{-1}$
$K$	turbulent diffusion coefficient	$\text{m}^2\text{s}^{-1}$
$L$	characteristic spatial scale of mixing	m



$L_w$	latent heat for liquid water	$\text{J kg}^{-1}$
$N$	droplet concentration	$\text{m}^{-3}$
$N_0$	Parameter of Gamma distribution	$\text{m}^{-3}$
$\bar{N}$	mean droplet concentration	$\text{m}^{-3}$
$N_1$	initial droplet concentration in cloud volume	$\text{m}^{-3}$
$p$	pressure of moist air	$\text{N m}^{-2}$
$q_v$	water vapor mixing ratio (mass of water vapor per 1 kg of dry air)	-
$q_w$	liquid water mixing ratio (mass of liquid water per 1 kg of dry air)	-
$q_{w1}$	liquid water mixing ratio in cloud volume	-
$R$	$\frac{S_2}{A_2 q_{w1}}$ , non-dimensional parameter	-
$R_a$	specific gas constant of moist air	$\text{J kg}^{-1}\text{K}^{-1}$
$R_v$	specific gas constant of water vapor	$\text{J kg}^{-1}\text{K}^{-1}$
$r$	droplet radius	m
$r_1$	initial droplet radius	m
$r_e$	effective radius	m
$r_{e0}$	initial effective radius	m
$S$	$e/e_w - 1$ , supersaturation over water	-
$S_2$	initial supersaturation in the dry volume	-
$S_0$	initial supersaturation in homogeneous mixing	-
$T$	temperature	K
$t$	time	s
$x$	distance	m
$\alpha$	parameter of Gamma distribution	-



$\beta$	parameter of Gamma distribution	$\text{m}^{-1}$
$\Delta t$	time step	s
$\mu$	cloud fraction	-
$\mu_{cr}$	critical cloud fraction	-
$\varepsilon$	turbulent dissipation rate	$\text{m}^2\text{s}^{-3}$
$\Gamma(x, t)$	conservative function	-
$\rho_a$	air density	$\text{kg m}^{-3}$
$\rho_w$	liquid water density	$\text{kg m}^{-3}$
$\sigma$	square of droplet radius	$\text{m}^2$

543

544

545

546

547

548

549

550

551

552

553

554

555

556

557

558

559



560

561 **References**

562 Boffetta, G. and Sokolov, I. M., 2002: Relative dispersion in fully developed turbulence:  
563 The Richardson's law and intermittency correction, *Phys. Rev. Lett.*, **88**, 094501,  
564 doi:10.1103/PhysRevLett.88.094501.

565 Burnet, F., and J.-L. Brenguier, 2007: Observational study of the entrainment-mixing  
566 process in warm convective cloud, *J. Atmos. Sci.*, **64**, 1995–2011.

567 Freud, E., D. Rosenfeld, and J. R. Kulkarni, 2011: Resolving both entrainment mixing and  
568 number of activated CCN in deep convective clouds, *Atmos. Chem. Phys.*, **11**, 12,887–12,900,  
569 doi:10.5194/acp-11-12887-2011.

570 Gerber H, Frick G, Jensen J.B, and Hudson J.G., 2008: Entrainment, mixing, and  
571 microphysics in trade-wind cumulus. *J. Meteorol. Soc. Jpn.*, **86A**. 87-106.

572 Knight C. A. and L. J. Miller, 1998: Early radar echoes from small, warm cumulus:  
573 Bragg and hydrometeor scattering. *J. Atmos. Sci.*, **55**, 2974-2992.

574 Korolev, A.V., 1995: The influence of supersaturation fluctuations on droplet size spectra  
575 formation. *J. Atmos. Sci.*, **52**, 3620-3634.

576 Korolev A., and I. Mazin, 2003: Supersaturation of water vapor in clouds, *J. Atmos. Sci.*,  
577 **60**, 2957-2974.

578 Korolev, A., Khain, A., Pinsky, M., and French, J., 2016: Theoretical study of mixing in  
579 liquid clouds – Part 1: Classical concept, *Atmos. Chem. Phys.*, **16**, 9235–9254.

580 Kovetz, A., and B. Olund, 1969: The effect of coalescence and condensation on rain  
581 formation in a cloud of finite vertical extent. *J. Atmos. Sci.*, **26**, 1060–1065.

582 Krueger, S. K., Lehr, P. J., & Su, C. W., 2006: How entrainment and mixing scenarios  
583 affect droplet spectra in cumulus clouds. In *12th Conference on Cloud Physics, and 12th*  
584 *Conference on Atmospheric Radiation*, Madison, WI.



585 Lehmann, K., H. Siebert, and R. A. Shaw, 2009: Homogeneous and inhomogeneous  
586 mixing in cumulus clouds: Dependence on local turbulence structure. *J. Atmos. Sci.*, **66**, 3641-  
587 3659.

588 Monin, A.S. and Yaglom, A.M. 1975: “Statistical Fluid Mechanics: Mechanics of  
589 Turbulence”, vol. **2**, MIT Press.

590 Pinsky, M., Khain, A., Korolev, A., and Magaritz-Ronen, L., 2016a: Theoretical  
591 investigation of mixing in warm clouds – Part 2: Homogeneous mixing, *Atmos. Chem. Phys.*,  
592 **16**, 9255–9272.

593 Pinsky, M., Khain, A., and Korolev, A., 2016b: Theoretical analysis of mixing in liquid  
594 clouds – Part 3: Inhomogeneous mixing, *Atmos. Chem. Phys.*, **16**, 9273–9297.

595 Polyanin A. D. and V. F. Zaitsev, 2004: Handbook of nonlinear partial differential  
596 equations. Chapman & Hall/CRC, 809 pp.

597 Pruppacher, H.R., Klett, J.D., 1997. Microphysics of Clouds and Precipitation. 2nd edn.  
598 Oxford Press, 914 p.

599

600

601

602

603

604

605

606

607

608

609

610



611

612

613

614

615

616 **Tab.1** Parameters of the initial Gamma distributions

DSD	$N_0$ , cm <sup>3</sup>	$\alpha$	$\beta$ , $\mu\text{m}$	Modal radius, $\mu\text{m}$	LWC, g/m <sup>3</sup>
Narrow	264.2	101.0	0.1	10.0	1.178
Wide	71.0	4.3	3.1	10.0	1.178

617

618

619

620

621

622

623

624

625

626

627

628

629

630

631

632

633



634

635

636

637

638

639

640

641

642

643

644

645

646

647

648

649

650 **Fig.1.** The initial state at  $t=0$ . The left volume is a saturated cloudy volume; the right

651 volume is an under-saturated dry air volume.

652

653

654

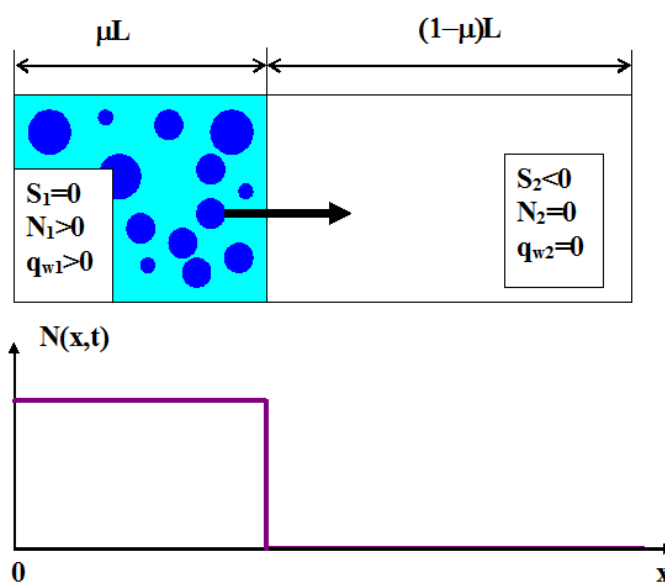
655

656

657

658

659





660

661

662

663

664

665

666

667

668

669

670

671

672

673

674

675

676

677

678

679

680

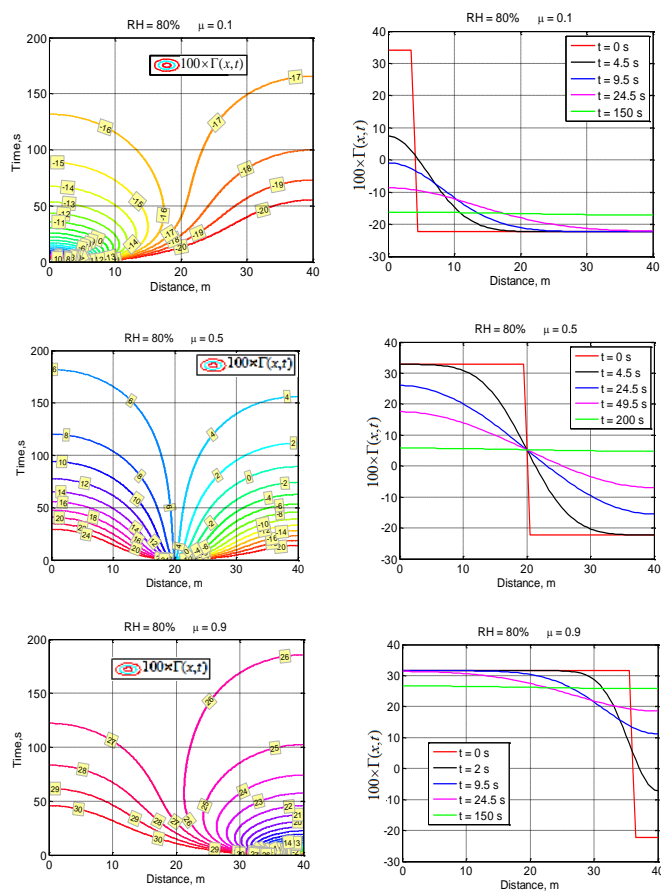
681

682 **Fig. 2.** Spatial-temporal variations of conservative function  $100 \times \Gamma(x, t)$  for different cloud

683 fractions  $\mu$  and initial  $RH_2 = 80\%$ .

684

685





686

687

688

689

690

691

692

693

694

695

696

697

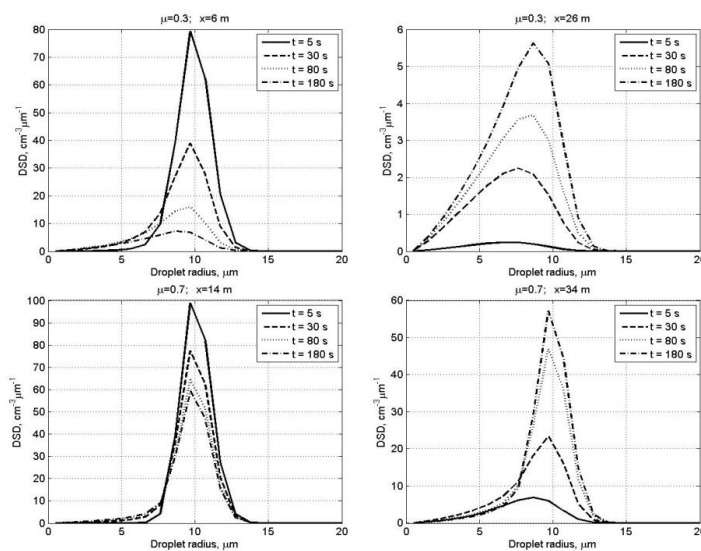
698

699

700

701

702



703

704

705

706

707

708

709

710

711

**Fig. 3.** Time evolution of DSD in the centers of the initially cloudy volume (left) and of the initially dry air volume (right) at initially narrow DSD. The initial mixing parameters are  $RH_2 = 80\%$ ,  $T = 10^\circ\text{C}$ ,  $p = 8288\text{ mb}$  and  $L = 40\text{ m}$ .



712

713

714

715

716

717

718

719

720

721

722

723

724

725

726

727

728

729

730

731 **Fig. 4.** The same as in Fig. 3, but for the initially wide DSD.

732

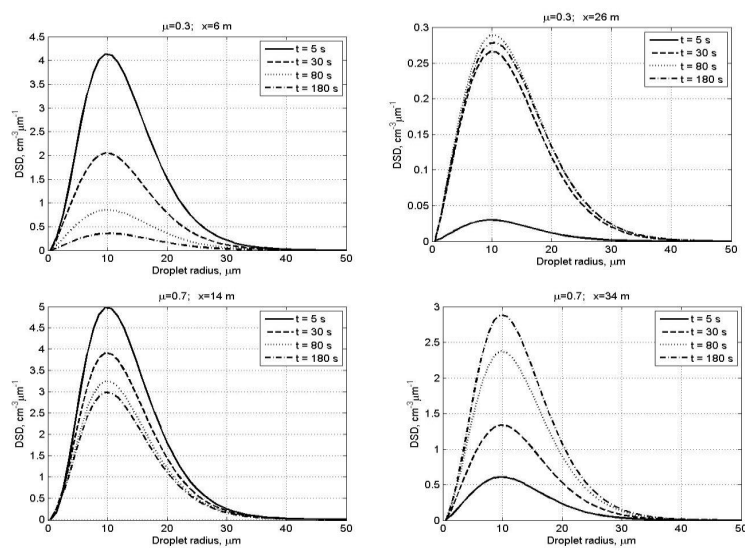
733

734

735

736

737





738

739

740

741

742

743

744

745

746

747

748

749

750

751

752

753

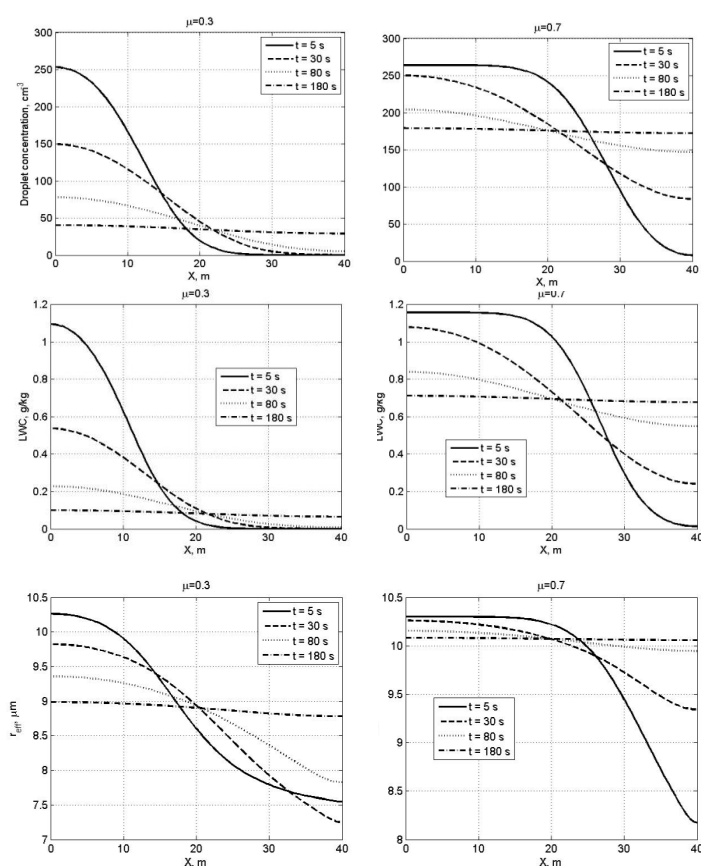
754

755

756

757

758



759 **Fig. 5.** Spatial dependences of droplet concentration, LWC and the effective radius within the  
760 mixing volume at different time instances at narrow initial DSD. The initial mixing  
761 parameters are  $RH_2 = 80\%$ ,  $T = 10^\circ\text{C}$ ,  $p = 8288\text{ mb}$  and  $L = 40\text{ m}$ .

762

763



764

765

766

767

768

769

770

771

772

773

774

775

776

777

778

779

780

781

782

783

784 **Fig. 6.** The same as in Fig. 5, but for wide DSD

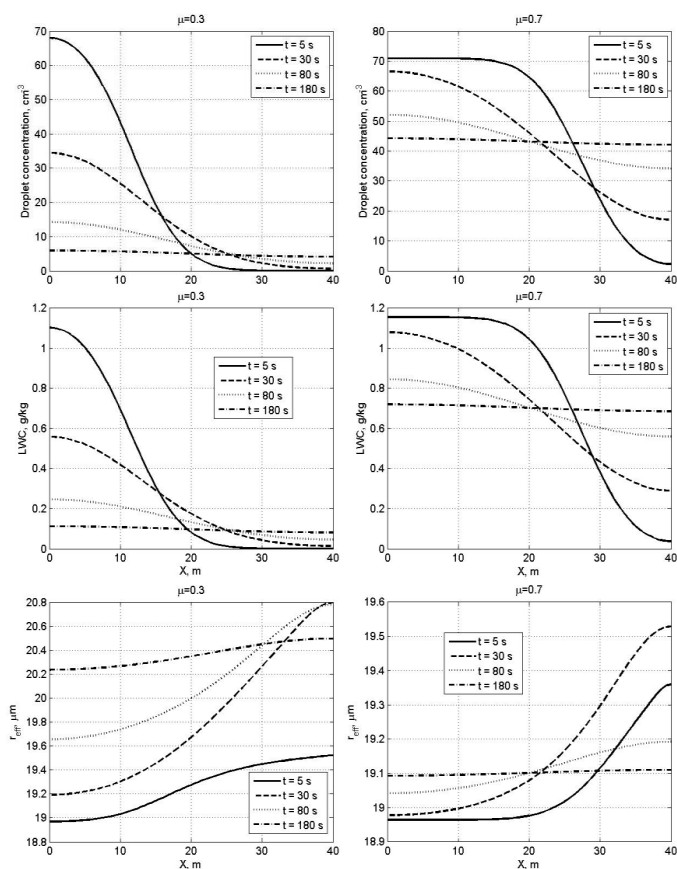
785

786

787

788

789





790

791

792

793

794

795

796

797

798

799

800

801

802

803

804

805

806

807

808

809

810

811

812

813

814

815

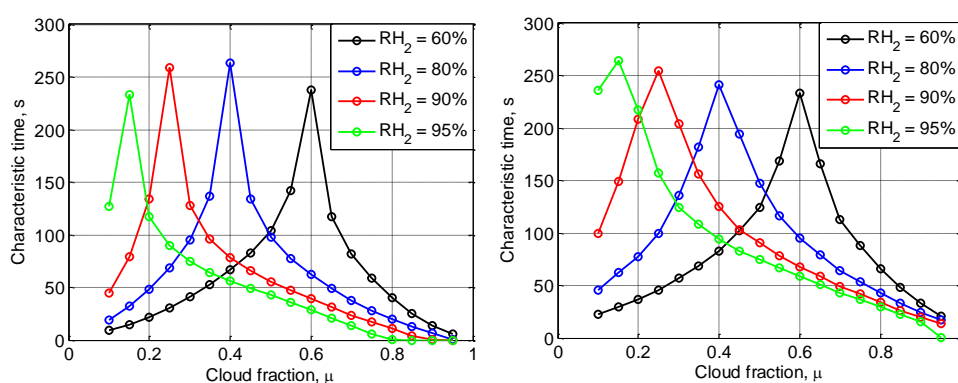


**Fig. 7.** Time required to reach the equilibrium state vs. the cloud fraction at different initial RH for the initially narrow DSD (left) and the initially wide DSD (right). Parameters of DSD are given in Tab. 1. The initial mixing parameters are  $T = 10^{\circ}\text{C}$ ,  $p = 8288$  mb and  $L = 40$  m.



816

817

818

819

820

821

822

823

824

825

826

827

828

829

830 **Fig. 8.** Dependences of normalized cube of the effective radius on the cloud fraction at831 different time instances for  $x=0$  (solid lines) corresponding to the initially cloud volume,832 and  $x=L$  (dash line) corresponding to the initially dry volume. The time instances in seconds

833 are marked by numbers. The figure is plotted for the narrow initial DSD for two values of

834  $RH_2$ : 60% (left panel) and 95% (right panel). Parameters of DSD are given in Tab. 1. The835 initial mixing parameters are  $T=10^\circ\text{C}$ ,  $p=8288$  mb and  $L=40$  m. Calculations performed836 within the range of  $0.1 < \mu < 0.95$ .

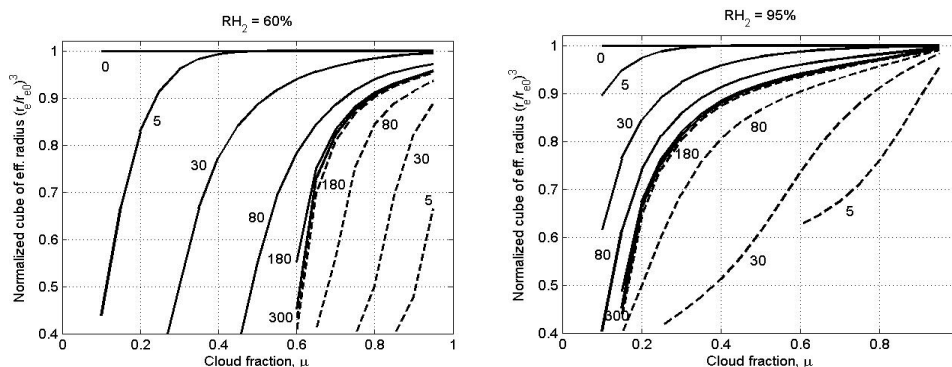
837

838

839

840

841





842

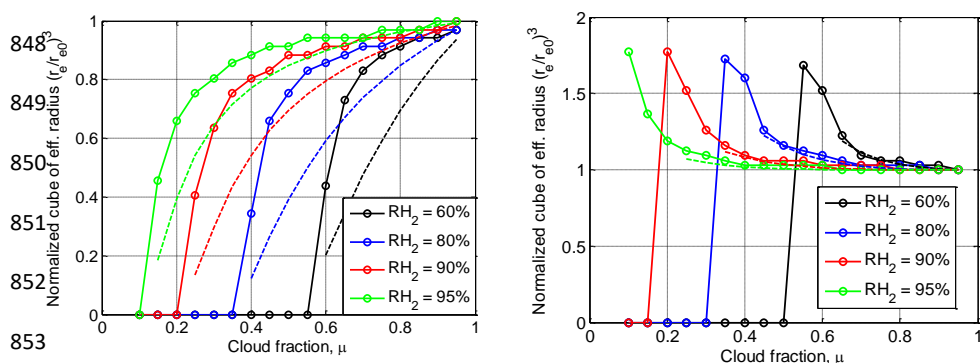
843

844

845

846

847



854

855 **Fig. 9.** Mixing diagrams. Normalized cube of the effective radius vs. the cloud fraction for  
856 initial narrow DSD (left) and initial wide DSD (right). The dependencies correspond to the  
857 equilibrium state Parameters of initial DSD are presented in Tab. 1. Solid and dashed lines  
858 show the mixing diagrams for inhomogeneous and homogeneous mixing, respectively. The  
859 initial mixing parameters are  $T = 10^\circ\text{C}$ ,  $p = 8288$  mb and  $L = 40$  m.

860

861

862

863

864

865

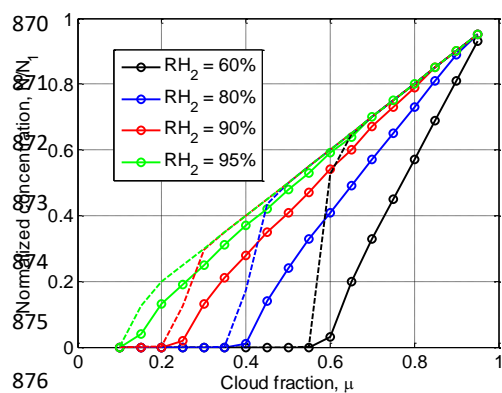
866

867



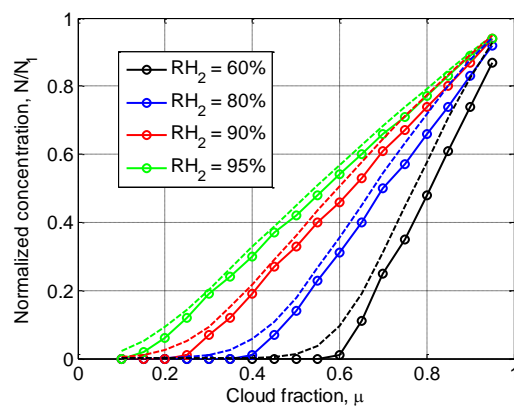
868

869



876

877



878

879

880

881

882

883

884

885

886

887

888

889

890

891

892

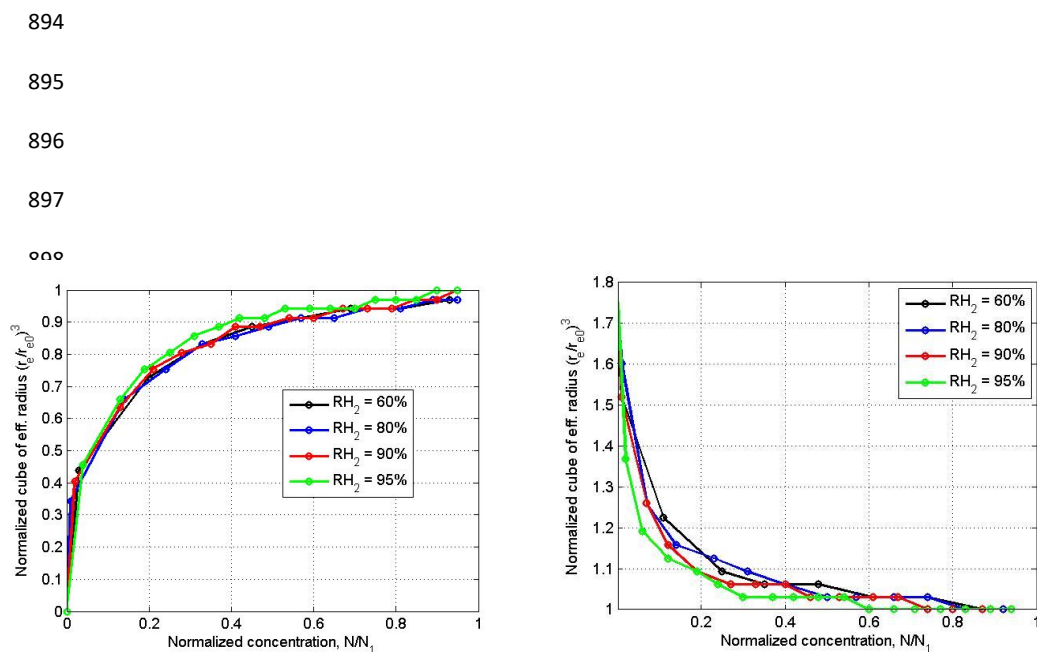
893

**Fig. 10.** Final normalized droplet concentration vs. cloud fraction for initially narrow DSD

(left) and initially wide DSD (right). Parameters of initial DSD are shown in Tab. 1. Dashed

line shows the results of equivalent homogeneous mixing. The initial mixing parameters are

$T = 10^\circ\text{C}$ ,  $p = 8288$  mb and  $L = 40$  m.



905

906 **Fig. 11.** Dependencies of normalized cube of the effective radius on normalized droplet

907 concentration for different initial relative humidity values. Left panel: narrow initial DSD.

908 Right panel: wide initial DSD. The initial mixing parameters are  $T = 10^\circ\text{C}$ ,  $p = 8288$  mb

909 and  $L = 40$  m.

910

911

912

913

914

915